SUPPLEMENTARY INFORMATION

Lithium nitridonickelate as anode coupled with argyrodite electrolyte for all-solid-state lithium-ion batteries

Yaxin Qu[1], Mickael Mateos[1,*], Nicolas Emery[1], Fermin Cuevas[1], Dimitri Mercier[2], Sandrine Zanna[2], Agustin Rios de Anda[1], Junxian Zhang[1]

(1) Univ Paris-Est Creteil, CNRS, ICMPE (UMR 7182), 2 rue Henri Dunant, F-94320 Thiais, France

(2) PSL Research University, CNRS – Chimie ParisTech, Institut de Recherche de Chimie Paris, Physical Chemistry of Surfaces Group, 11 Rue Pierre et Marie Curie, 75005 Paris, France

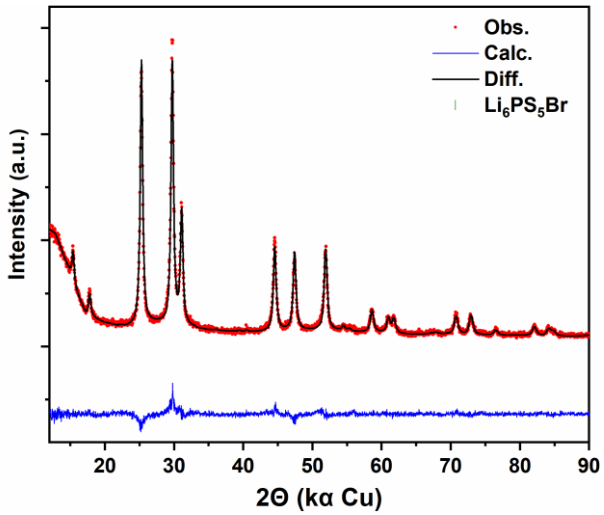

Figure S1. XRPD pattern in 2Θ (Cu Kα) and corresponding Rietveld refinement of the ball-milled Li_6PS_5Br sample.

SEM micrographs of ball-milled argyrodite reveal poor crystallinity, characterized by irregular particles and agglomerates ranging in size from a few hundred nanometers to ten micrometers (Figure S2).

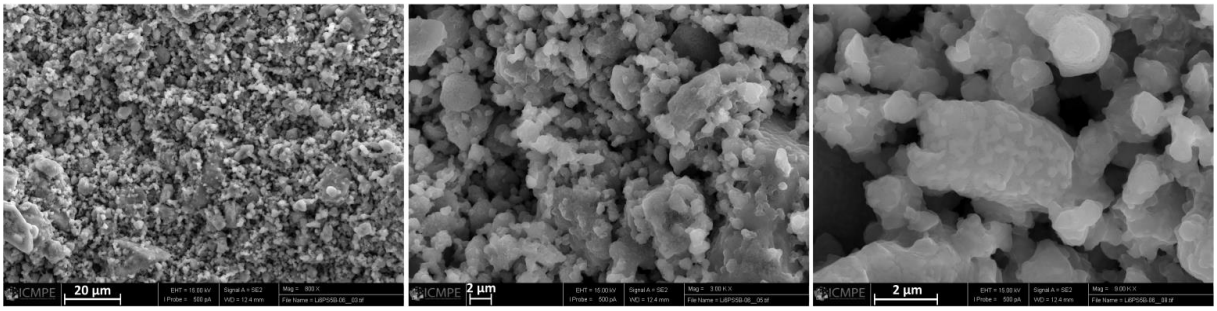

Figure S2: SEM micrographs at different magnifications of balled-milled Li_6PS_5Br argyrodite

For Solid-state NMR based on ^7Li spin-lattice relaxation (SLR) measurements approximately 100 mg of argyrodite was transferred in a glovebox to a 4 mm ZrO_2 MAS rotor (Cortecnet). All of the experiments were conducted on a Bruker Avance III 400 MHz equipped with a MAS II spinning unit and a BVT 3000 heating unit. Samples were tested on a CP-MAS DVT 4mm low-γ ^1H-X probe, which was set on the X channel at 155.506 MHz for ^7Li detection. Samples were spun at 6 kHz with a temperature stabilization of 30 minutes prior to measuring. The ^7Li nuclei were directly magnetized without the need of cross-polarization. The delay pulse time was of 2 s for all samples and temperatures. The pulse sequence used in this work to obtain the T_1 relaxation times is a derivative of a classic inversion recovery sequence and was optimized by Hanghofer et al. [1] which includes a train of ten $\pi/2$ impulsions acting as dipolar filters in between the initial excitation impulsion and the FID acquisition. Each impulsion is separated by a delay time of 20 ms. The inversion recovery delay period after the dipolar filter train τ was varied between 0.04 and 1000 ms. 3000 scans per sample per temperature per inversion recovery delay period τ where acquired. To obtain the T_1 values for a given temperature, the normalized intensity of each measurement was plotted as a function of τ, with T_1 being obtained from a single exponential fit.

To probe the local Li-ion temperature dependent mobility, ^7Li static spin–lattice relaxation (SLR) rates in the laboratory frame, $R_1 = 1/T_1$, is plotted versus 1000/T (Figure S3). Indeed, assuming an Arrhenius behavior for the Li-ion residence time, i.e. $T_1 = T_{1,0}e^{-E_a/K_bT}$, the slope of the SLR rates can be related to the activation energy for the Li-ion motional processes. Over a large domain of temperature, a BPP behavior should-be expected in the form of a pseudo-Lorentzian, but the present data are not sufficient to obtain such behavior a larger temperature domain is required (200 to 450K).[1,2] A linear fitting gives an activation energy of 0.37(3) eV for the balled-milled argyrodite, not so far to the one obtained with impedance spectroscopy and published data at 0.29 eV, ascribed to long-range Li-ion diffusion processes.[3] However, this value are far from higher than the one obtained by Hanghofer et al. at 0.21 eV[1] and Yu et al. at 0.15 eV[2]

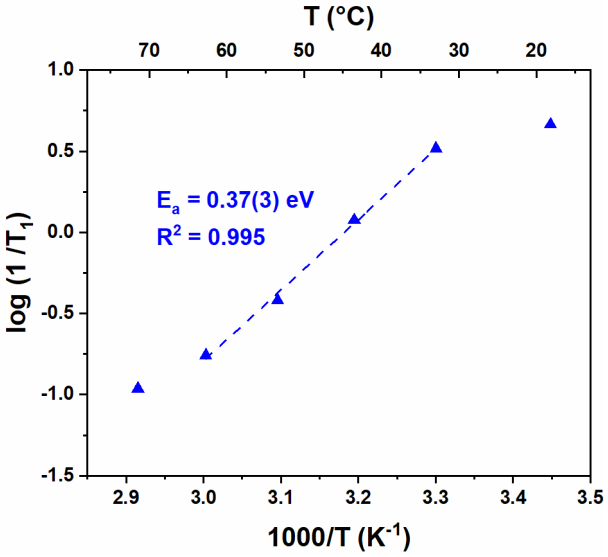

Figure S3: Temperature dependence of the diffusion-induced ^{7}Li NMR spin–lattice relaxation rates R1 of Li_6PS_5Br.

Chrono-potentiometry at a constant potential of 0.5 V was performed on a ball-milled argyrodite pellet to assess its electronic conductivity (Figure S4). Based on the measured current and the pellet's geometry, the electronic conductivity was estimated to be $5 \pm 1\ 10^{-9}$ S.cm^{-1}, which is five orders of magnitude lower than its ionic conductivity.

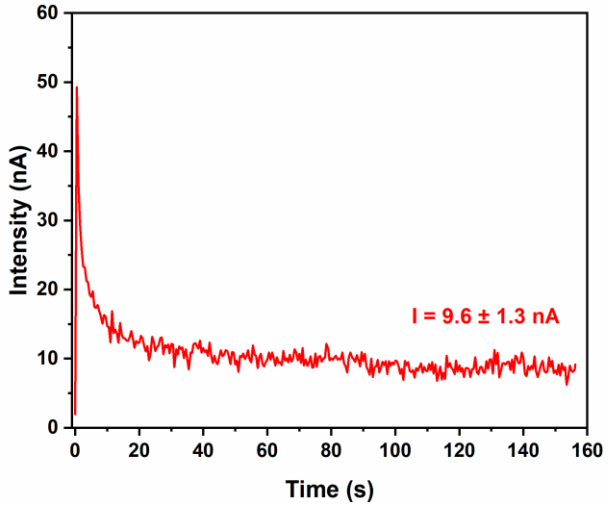

Figure S4: Evolution of the current under continuous polarization of 0.5 V for a balled-milled argyrodite pellet (S = 0.283 cm², e = 0.8 mm).

The electrochemical stability window (ESW) of bromide argyrodite was determined through two separate cyclic voltammetry experiments at a scan rate of 0.1 mV s^{-1} (Figure S5). The first experiment was conducted at low potential (0–2 V) and the second at high potential (1.5– 5 V), using a composite made up of 25 wt.% CVGF and 75 wt.% Li_6PS_5Br to enhance the electrochemical response of argyrodite [4], which is an electronic insulator. At low potential, the cathodic current starts to increase at 0.9 V, leading to a massive cathodic peak at 0.1 V. Upon the reverse scan, a broad anodic peak is observed at 0.2 V. This broad, reversible signal remains relatively stable over cycling (see cycle 2 dotted line) and is attributed to the multi-step reversible reduction of phosphorus from $P^{(V)}$ to $P^{(-III)}$ [5–7]. At high potential, the anodic current begins to rise at 2.5 V, leading to two anodic peaks at 2.8

V and 3.5 V. Upon the reverse scan, a weak cathodic peak appears at 1.9 V. This quasi-irreversible signal declines significantly after cycling (see cycle 2, dotted line), and is associated with the irreversible oxidation of sulfur from $S^{(-II)}$ to $S^{(0)}$ and also oxidation of the PS_4^{3-} unit through a possible large variety of thiophosphate species like $P_2S_7^{4-}$, $P_2S_6^{2-}$ [4,5,7,8]. Thus, the ESW of this solid electrolyte extends from 0.9 V to 2.5 V. However, it should be noted that this narrow ESW is observed with a high carbon additive content to exacerbate and better characterize argyrodite degradation. These operation conditions are not used in real devices. Therefore, the use of electrode materials with operating potentials outside this window cannot be ruled out, such as Li-In alloy (0.6 V) for the anode, or $LiFePO_4$ or NMC for the cathode [9,10].

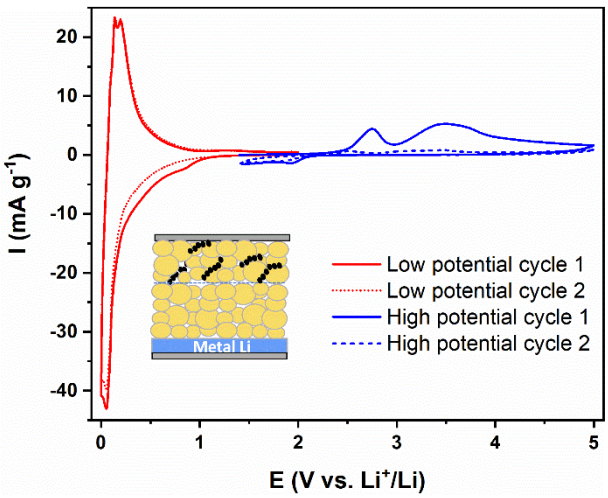

Figure S5: Two cyclic voltammograms of Li_6PS_5Br-CVGF | Li_6PS_5Br | Li half-cell recorded at 0.1 mV s^{-1} withing the potential range of 0 – 2 V (red) and 1.5 – 5 V (blue)

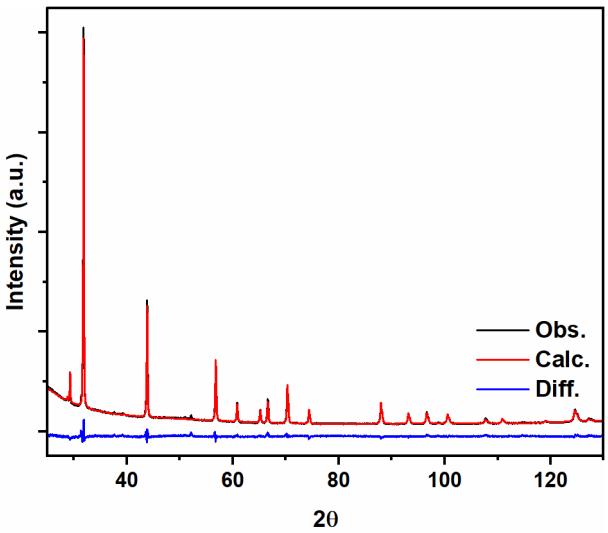

Figure S6 Rietveld refinement of the $Li_{2.07}Ni_{0.62}N$ XRPD pattern in 2θ with Co Kα

The EDX chemical mapping of the $Li_{2.1}Ni_{0.62}N$ (45 wt.%) / CVGF (5 wt.%) / Li_6PS_5Br (50 wt.%) composite revealed a relatively homogeneous mixture (Figure S6). The argyrodite phase was easily identified by the concomitance of Br, S, and P regions, while the nitride phase was identified by the

presence of N and Ni regions. The argyrodite surrounds the nitride particles and forms a percolate network that facilitates lithium diffusion. Due to surface contamination, carbon is not easily identified through chemical mapping. However, backscattered electron images (Figure S6f) clearly show the presence of fibers originating from the Carbon Vapor Growth Fiber (CVGF).

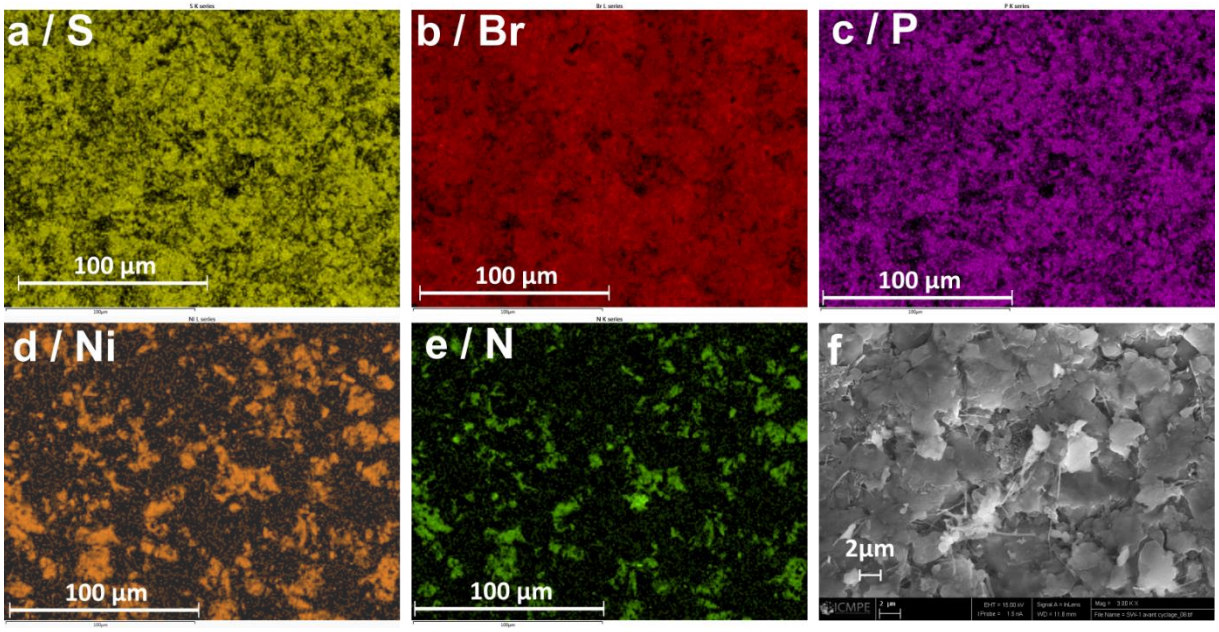

Figure S7: Chemical mapping of $Li_{2.1}Ni_{0.62}N$ (45 wt.%) / CVGF (5 wt.%) / Li_6PS_5Br (50 wt.%) composite with a) S (K-edge), b) Br (L-edge), c) P (K-edge), d) Ni (L-edge), e) N (K-edge), f) back-scatered electron micrograph.

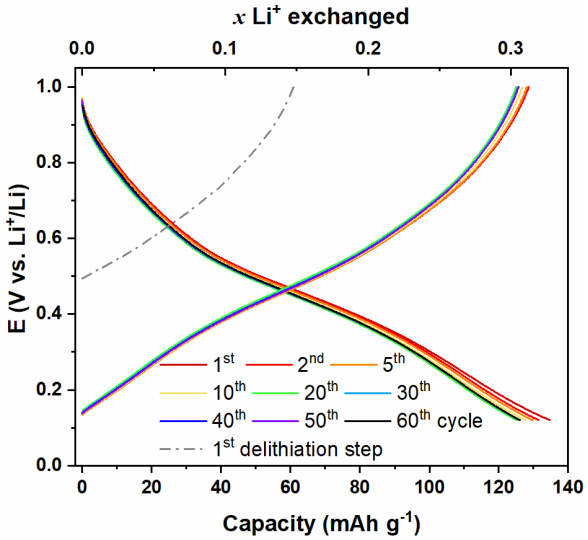

Figure S8: Evolution of the potential profile as a function of cycle number for the $Li_{2.07}Ni_{0.62}N$ | Li_6PS_5Br | Li half-cell at 8 mA g^{-1} (~C/25) withing the potential range of 0.12-1V.

To evaluate the electrochemical compatibility of the active material and solid electrolyte, Figure S9 compares the galvanostatic cycling of nitride using bromide or chloride argyrodite as the solid electrolyte." The sloping potential profiles are quite similar; however, for the chloride argyrodite, the

coulombic efficiency is lower throughout the cycling, resulting in increased hysteresis and a loss of reversible capacity.

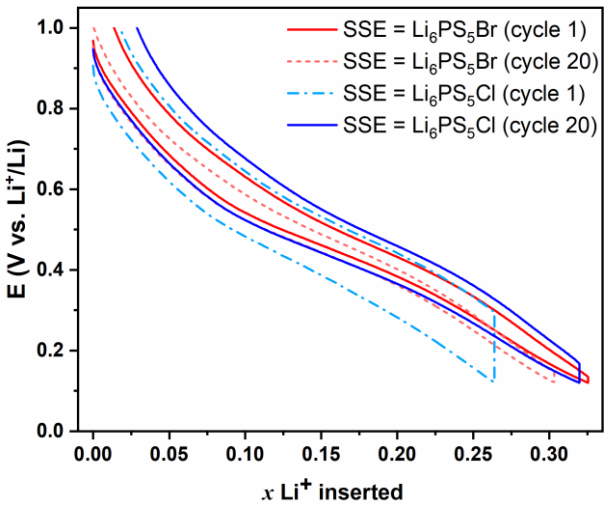

Figure S9: Long-term cycling of the $Li_{2.07}Ni_{0.62}N$ composite | Li_6PS_5X | Li half-cell (X = Br in red and X = Cl in blue) at 8 mA g^{-1} (C/25) within 0.12 – 1 V potential window. Only cycles 1 (solid line) and 20 (dotted line) are displayed.

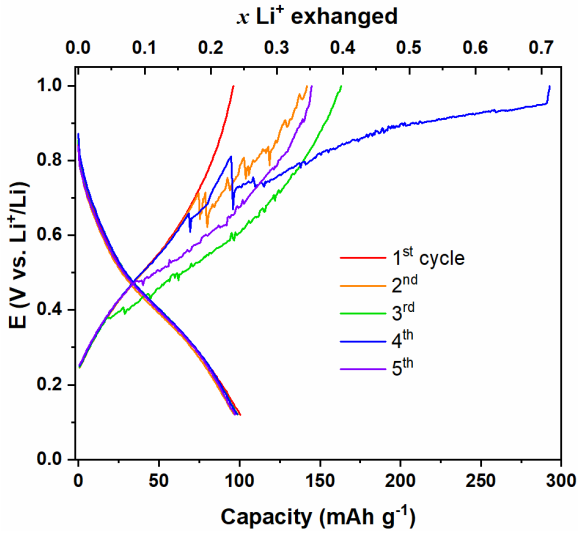

Figure S10: Battery failure upon delithiation: evolution of the potential profile for the $Li_{2.07}Ni_{0.62}N$ | Li_6PS_5Br | Li half-cell at 40 mA g^{-1} (~C/5) withing the potential range of 0.12-1V.

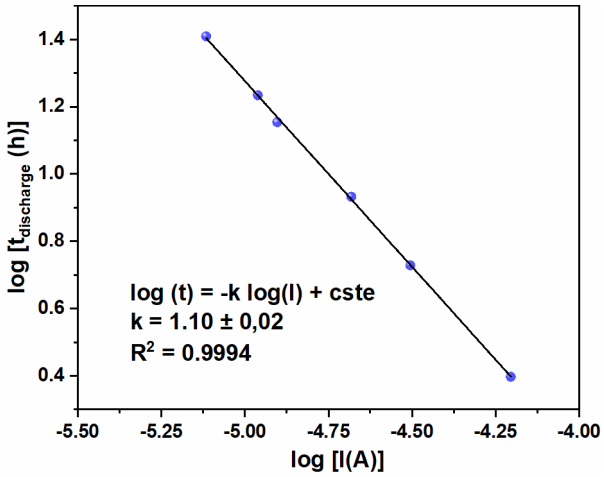

Figure S11: Peukert plot from galvanostatic data at currents of 4.9, 6.5, 8, 13, 20 and 40 mA g^{-1}

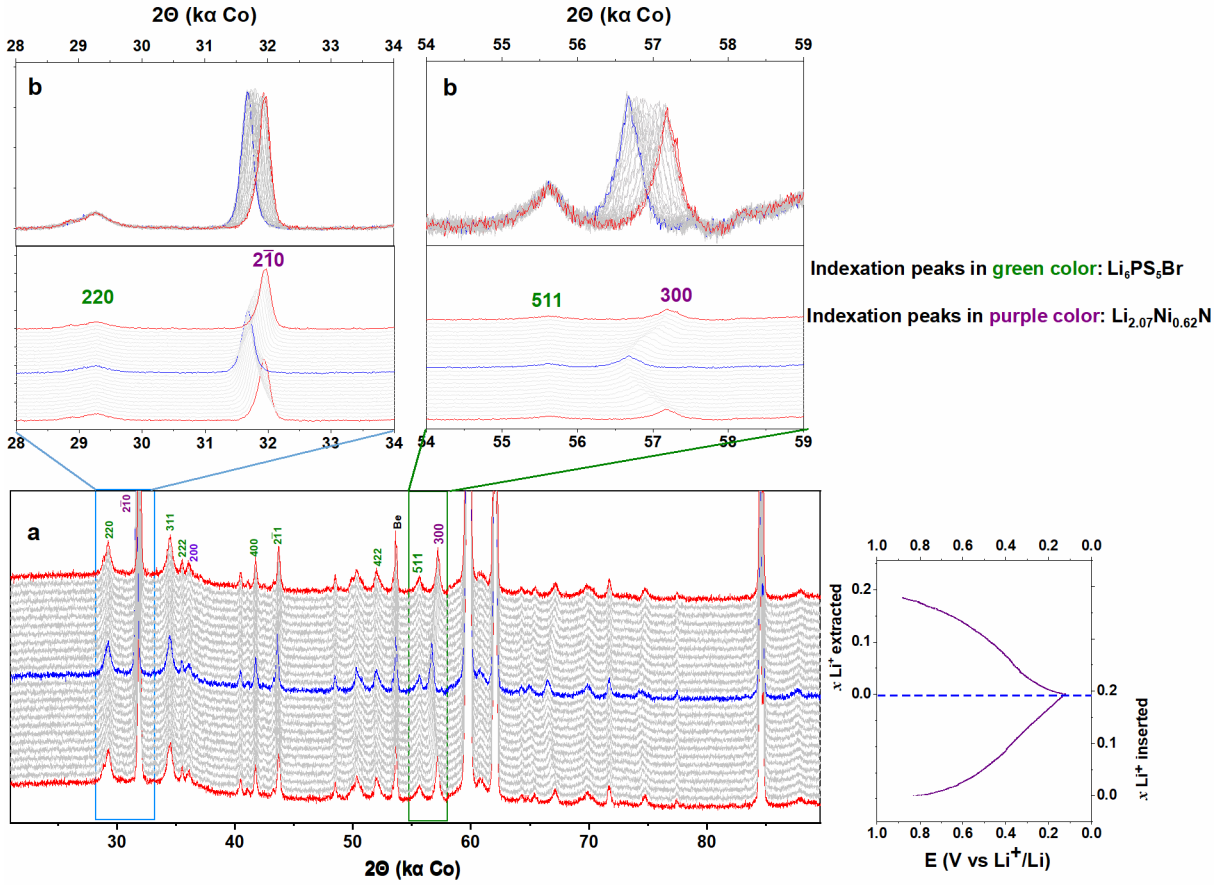

Figure S12**:** Operando XRD in 2Θ during galvanostatic cycling with (a) XRD patterns at different charge states, starting from delithiated nitride ($x_{inserted}$ = 0, pattern in red at the bottom), reaching lithiated nitride (x_{inserted} = 0.2, pattern in blue in the middle), and returning to delithiated nitride ($x_{\text{extracted}}$ = 0.2, pattern in red at the top). (b) Zoomed view of the displacement of the (300) and (2$\bar{1}$0) diffraction peaks for $Li_{2.07}Ni_{0.62}N$, and the (220) and (511) diffraction peaks for the bromide argyrodite.

Table 1 : Review of anode material performances for Li-ion batteries using liquid electrolyte

Material	Lithiated phase	Capacity (mAh g^{-1})	Mean working potential (V vs. Li^+/Li)	volume change (%)	ref
Graphite	LiC_6	372	0.1	12	X
Sn	$Li_{4.4}Sn$	993	0.6	260	X
Si	$Li_{4.4}Si$	4200	0.4	410	X
$Li_4Ti_5O_{12}$	$Li_7Ti_5O_{12}$	175	1.6	1	X
$Li_2Ni_{0.67}N$	$Li_{2.17}Ni_{0.67}N$	200	0.5	2	X
Li_7MnN_4	Li_7MnN_4	240	1.1	7	X

References

[1] I. Hanghofer, M. Brinek, S.L. Eisbacher, B. Bitschnau, M. Volck, V. Hennige, I. Hanzu, D. Rettenwander, H.M.R. Wilkening, Substitutional disorder: structure and ion dynamics of the argyrodites Li_6PS_5Cl, Li_6PS_5Br and Li_6PS_5I, Phys. Chem. Chem. Phys. 21 (2019) 8489–8507.

[2] C. Yu, S. Ganapathy, E.R.H. van Eck, L. van Eijck, S. Basak, Y. Liu, L. Zhang, H. W. Zandbergen, M. Wagemaker, Revealing the relation between the structure, Li-ion conductivity and solid-state battery performance of the argyrodite Li_6PS_5Br solid electrolyte, J. Mater. Chem. A 5 (2017) 21178–21188.

[3] C. Yu, S. Ganapathy, N.J.J. de Klerk, I. Roslon, E.R.H. van Eck, A.P.M. Kentgens, M. Wagemaker, Unravelling Li-Ion Transport from Picoseconds to Seconds: Bulk versus Interfaces in an Argyrodite Li_6PS_5Cl–Li_2S All-Solid-State Li-Ion Battery, J. Am. Chem. Soc. 138 (2016) 11192–11201.

[4] G.F. Dewald, S. Ohno, M.A. Kraft, R. Koerver, P. Till, N.M. Vargas-Barbosa, J. Janek, W.G. Zeier, Experimental Assessment of the Practical Oxidative Stability of Lithium Thiophosphate Solid Electrolytes, Chem. Mater. 31 (2019) 8328–8337.

[5] L. Zhou, N. Minafra, W.G. Zeier, L.F. Nazar, Innovative Approaches to Li-Argyrodite Solid Electrolytes for All-Solid-State Lithium Batteries, Acc. Chem. Res. 54 (2021) 2717–2728.

[6] S. Wenzel, S.J. Sedlmaier, C. Dietrich, W.G. Zeier, J. Janek, Interfacial reactivity and interphase growth of argyrodite solid electrolytes at lithium metal electrodes, Solid State Ion. 318 (2018) 102–112.

[7] D.H.S. Tan, E.A. Wu, H. Nguyen, Z. Chen, M.A.T. Marple, J.-M. Doux, X. Wang, H. Yang, A. Banerjee, Y.S. Meng, Elucidating Reversible Electrochemical Redox of Li_6PS_5Cl Solid Electrolyte, ACS Energy Lett. 4 (2019) 2418–2427.

[8] R. Koerver, F. Walther, I. Aygün, J. Sann, C. Dietrich, W.G. Zeier, J. Janek, Redox-active cathode interphases in solid-state batteries, J. Mater. Chem. A 5 (2017) 22750–22760.

[9] T. Kim, K. Kim, S. Lee, G. Song, M.S. Jung, K.T. Lee, Thermal Runaway Behavior of Li_6PS_5Cl Solid Electrolytes for $LiNi_{0.8}Co_{0.1}Mn0.1O_2$ and $LiFePO_4$ in All-Solid-State Batteries, Chem. Mater. 34 (2022) 9159–9171.

[10] L. Peng, C. Yu, Z. Zhang, H. Ren, J. Zhang, Z. He, M. Yu, L. Zhang, S. Cheng, J. Xie, Chlorine-rich lithium argyrodite enabling solid-state batteries with capabilities of high voltage, high rate, low-temperature and ultralong cyclability, Chem. Eng. J. 430 (2022) 132896.